tvst

Article

3D Microstructure of the Healthy Non-Human Primate Lamina Cribrosa by Optical Coherence Tomography Imaging

Anoop Sainulabdeen[1,*], Yoav Glidai[1,*], Mengfei Wu[1,2], Mengling Liu[2], Palaiologos Alexopoulos[1], Hiroshi Ishikawa[1,3], Joel S. Schuman[1,3,4], and Gadi Wollstein[1,3,4]

[1] Department of Ophthalmology, NYU Langone Health, New York, NY, USA
[2] Division of Biostatistics, Departments of Population Health and Environmental Medicine, NYU Langone Health, New York, NY, USA
[3] Department of Biomedical Engineering, NYU Tandon School of Engineering, Brooklyn, NY, USA
[4] Center for Neural Science, NYU, New York, NY, USA

Correspondence: Gadi Wollstein, Department of Ophthalmology, NYU Langone Health, 222 East 41st Street, New York, NY 10017, USA.
e-mail: gadi.wollstein@nyulangone.org

Received: September 29, 2020
Accepted: March 23, 2022
Published: April 18, 2022

Keywords: optical coherence tomography (OCT); non-human primate (NHP); lamina cribrosa (LC)

Citation: Sainulabdeen A, Glidai Y, Wu M, Liu M, Alexopoulos P, Ishikawa H, Schuman JS, Wollstein G. 3D microstructure of the healthy non-human primate lamina cribrosa by optical coherence tomography imaging. Transl Vis Sci Technol. 2022;11(4):15, https://doi.org/10.1167/tvst.11.4.15

Purpose: The lamina cribrosa (LC) has an important role in the pathophysiology of ocular diseases. The purpose of this study is to characterize in vivo, noninvasively, and in 3D the structure of the LC in healthy non-human primates (NHPs).

Methods: Spectral-domain optical coherence tomography (OCT; Leica, Chicago, IL) scans of the optic nerve head (ONH) were obtained from healthy adult rhesus macaques monkeys. Using a previously reported semi-automated segmentation algorithm, microstructure measurements were assessed in central and peripheral regions of an equal area, in quadrants and depth-wise. Linear mixed-effects models were used to compare parameters among regions, adjusting for visibility, age, analyzable depth, graded scan quality, disc area, and the correlation between eyes. Spearmen's rank correlation coefficients were calculated for assessing the association between the lamina's parameters.

Results: Sixteen eyes of 10 animals (7 males and 3 females; 9 OD, 7 OS) were analyzed with a mean age of 10.5 $\pm$ 2.1 years. The mean analyzable depth was 175 $\pm$ 37 µm, with average LC visibility of 25.4 $\pm$ 13.0% and average disc area of 2.67 $\pm$ 0.45mm^2. Within this volume, an average of 74.9 $\pm$ 39.0 pores per eye were analyzed. The central region showed statistically significantly thicker beams than the periphery. The quadrant-based analysis showed significant differences between the superior and inferior quadrants. The anterior LC had smaller beams and pores than both middle and posterior lamina.

Conclusions: Our study provides in vivo microstructure details of NHP's LC to be used as the foundation for future studies. We demonstrated mostly small but statistically significant regional variations in LC microstructure that should be considered when comparing LC measurements.

Introduction

The lamina cribrosa (LC), a collagenous meshwork within the optic nerve head (ONH), is widely regarded as a key player in the pathogenesis of ocular diseases such as glaucoma.[1,2] Through the LC fenestrations, the retinal ganglion cell axons pass on their way from the retina to the brain. The mechanical theory of glaucomatous damage to the retinal ganglion cell axons hypothesizes that the damage is due to an altered biomechanical environment within the LC.[2] These mechanical forces mainly originate from the intraocular and intracranial pressures, distort the LC and cause a cascade of biological events, including reduced axoplasmic transport of neurotrophic factors, tissue hypoxia, and glial cell activation, resulting in neuronal cell death and impaired vision.[3–5] A thorough understanding of the in vivo, healthy 3D microstructure of the LC is essential to lay the foundation for any future work aimed at understanding changes due to disease state.

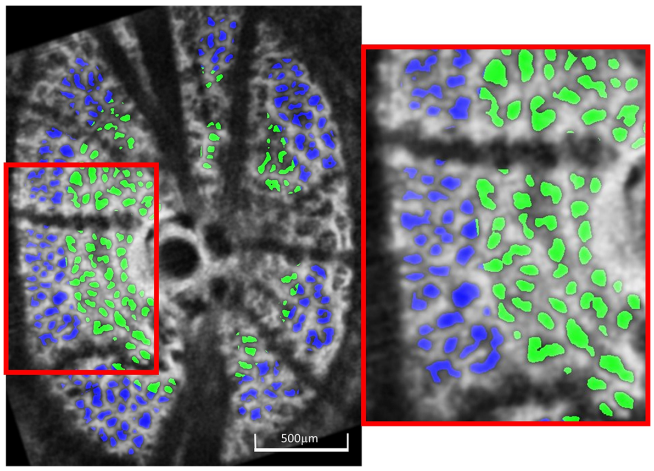

Figure. Semi-automated segmentation method delineating the lamina cribrosa pores. The scan has been pre-processed by smoothing and contrast enhancement. Central pores are colored in green and peripheral pores in blue.

The non-human primate (NHP) has become a well-established animal model for studying ocular diseases, as the NHP eye and visual pathway shares a close anatomic resemblance with humans.[6,7] A previous histomorphometric study in NHPs showed that beams and pores in the LC (Figure) remodeled differently by quadrant, depth, and from the center to periphery.[8] Although LC microstructure[9] and 3D histomorphometry[10] of healthy and early experimental glaucoma (EG) in postmortem specimens from NHPs have been reported, there is a knowledge gap on the 3D microstructure of LC in healthy live monkeys. Considering the postmortem changes in structure, such as elimination of blood pressure and the collapse of blood vessels typically occupying the LC beams, impairment to fluid balance and transportation, and tissue stiffening, in vivo analysis is imperative to determine the actual LC structure that is involved in disease mechanisms. Furthermore, in vivo, LC noninvasive characterization allows performing longitudinal studies to follow remodeling changes in given eyes. The purpose of this study is to characterize in vivo, noninvasively, and in 3D the LC microstructure of healthy NHPs.

Methods

Animals

Healthy adult rhesus macaque monkeys (Macaca mullata) that also participated in other non-related experiments were included in this study. These additional experiments did not affect the eyes, brain, or circulation. All procedures were approved by the University of Pittsburgh Institutional Animal Care and Use Committee (IACUC) and adhere to both the guidelines set by the National Institute of Health (NIH) and the Association for Research in Vision and Ophthalmology (ARVO) statement for the use of animals in ophthalmic research.

Anesthesia and Animal Preparation

Before the beginning of the experiment, IOP was measured with Perkins applanation tonometry and was 12.0 mm Hg (range = 10–14) in the right eye and 7.5 mm Hg (range = 8–12) in the left eye. Animals were anesthetized with ketamine (20 mg/kg) and midazolam (0.25 mg/kg), intubated, and the anesthesia was maintained with isoflurane (1 ± 3%) during scanning. In order to inhibit ocular movements during scanning, animals were paralyzed using vecuronium bromide (2 mg/hour) and ventilated to maintain an end-tidal CO_2 of approximately 35 mm Hg. An ophthalmic solution of tropicamide 0.5% was used to dilate the pupil and the animals were secured in a stereotaxic frame with the body in the prone position and the head held upright.

Optical Coherence Tomography Imaging

A gas permeable contact lens was applied to the eye before scanning to improve the image quality. An eye speculum was used to keep the eye open, and teardrops were applied every 5 minutes to prevent drying of the cornea. All eyes were scanned in a $3 \times 3 \times 1.6$ mm^3 volume ($512 \times 512 \times 1024$ pixels) centered on the ONH using a spectral-domain optical coherence tomography (OCT) device (Leica, Chicago, IL) with a scan rate of 20,000 A-scans/second. All scans were acquired within 30 minutes of induction of the anesthesia.

Image Analysis

All scans were graded for image quality and LC microstructural visibility by two qualified observers because the device provides no automated indicator. Scans graded as poor quality were excluded from the analysis. Scans were processed and analyzed using a method we previously described in detail.[11,12] In short, scans were made isotropic and smoothing was applied by using 3D-gaussian blur. Contrast-limited adaptive histogram equalization (CLAHE) image processing tool in FIJI (ImageJ)[13] was used to equalize local pixel intensity differences. Multiple combinations of these parameters were tested and the one subjectively perceived by two independent observers to best delineate the microstructure was chosen. A manually defined mask was applied to separate the visible

LC from the surrounding optic nerve head anatomy. An automated thresholding technique was then used to binarize the image, differentiating between pores and beams (Figure, Supplementary S1). LC visibility was determined by the ratio of visible LC, using c-mode maximum intensity projections, to the disc area, measured at the Bruch's membrane opening (BMO). Disc area and aspect ratio (long axis diameter divided by the perpendicular diameter) were measured by fitting an ellipse to the BMO. Microstructural measurements (beam thickness and pore diameter) were obtained using FIJI and BoneJ and averaged across the studied scan volume.[14] Beam thickness and pore diameter were calculated by measuring the best-fitting sphere's diameter in the given structure. Beam-to-pore ratio (BPR) was calculated as average beam thickness divided by average pore diameter. Mean pore area was measured as the mean value over a stalk of 2D planes where in each plane the number of pixels within pores was divided by the number of pores. The mean pore aspect ratio (AR) was computed by dividing the major and minor axes, measured by the best-fitting ellipse in each plane. The mean of the stalk of all planes was reported. Connective tissue volume fraction (CTVF) was computed as the number of voxels in the beams divided by the visible LCs. These parameters have been previously reported to be highly reproducible.[12]

All eyes were oriented for the right eye and quantified by quadrant, central versus peripheral, and depth. Quadrants were divided into 45/135 degrees bisectors through the BMO centroid. The area contained within the BMO was divided into two equal-area circles of the central and peripheral LCs (see the Figure). The visible LC of each eye was divided into equal thirds, generating the anterior, middle, and posterior regions. The thickness of the visible thirds varied between eyes depending on the thickness of the visible LC.

Statistical Analysis

Summary statistics were provided with mean and standard deviation. A linear mixed-effects model with a random intercept to account for intra-subject correlation was used to test the sectoral difference. The model was adjusted for covariates, such as age, analyzable depth, graded scan quality, visibility, and disc area. Spearman's rank correlation coefficient ρ was used to quantify the correlation between outcome measures for the entire LC region. Statistical analysis was performed using R software version 3.5.2. A P value less than 0.05 was considered statistically significant.

Results

Sixteen eyes (9 OD and 7 OS) of 10 healthy adult rhesus macaques qualified for the analysis. Seven animals were males, and three were females, with a mean age of 10.9 ± 2.3 years. The mean weight of the animals was 10.5 ± 2.9 kg.

Global LC Parameters

The mean disc area was 2.67 ± 0.45 mm^2 with a mean aspect ratio of 1.35 ± 0.14. Overall, LC visibility was 25.35 ± 13.02% with an average analyzable depth of 175.10 ± 37.64 µm ranging between 109.4 and 234.4 µm. The rest of the global parameters are listed in Table 1.

Center Versus Periphery

The central LC's microarchitecture had better visibility than the peripheral (31.0% vs. 20.7%). Beam thickness in the central LC was statistically significantly larger than in the periphery (33.08 vs. 30.11 µm,

Table 1. Global LC Microstructural Measurements and Comparison Between the Center and Periphery Measurements

Parameter	Global	Center	Periphery	P Value for Center vs. Periphery Center vs. Per
Beam thickness, µm	33.05 (3.04)	33.08 (3.08)	30.11 (4.02)	0.02*
Pore diameter, µm	21.46 (3.03)	21.52 (2.83)	20.06 (3.46)	0.14
Pore area, µm^2	875.97 (234.30)	834.44 (196.58)	838.88 (250.11)	0.93
Pore AR	1.93 (0.08)	1.96 (0.09)	2.00 (0.17)	0.52
BPR	1.56 (0.18)	1.56 (0.20)	1.48 (0.14)	0.30
CTVF, %	0.75 (0.03)	0.73 (0.04)	0.73 (0.05)	0.21

. Values are reported as mean (SD).
*Statistically significant.
AR, aspect ratio; BPR, beam-to-pore ratio; CTVF, connective tissue volume fraction.

Table 2. LC Microstructure Measurements in Quadrants

Parameter	Superior	Temporal	Inferior	*P* Value		
				Sup vs. Inf	Temp vs. Inf	Sup vs. Temp
Beam thickness, µm µm	30.91 (2.86)	33.95 (3.13)	30.30 (4.39)	0.36	0.28	0.66
Pore dimeter, µm	19.42 (2.27)	21.81 (3.19)	20.90 (3.18)	0.28	0.49	0.21
Pore area, μm^2	736.20 (198.29)	880.15 (254.36)	861.65 (232.5)	0.05	0.62	0.52
Pore AR	1.94 (0.11)	1.93 (0.07)	1.97 (0.14)	0.09	0.25	0.95
BPR	1.60 (0.14)	1.58 (0.19)	1.46 (0.16)	0.04*	0.51	0.53
CTVF, %	0.76 (0.03)	0.74 (0.04)	0.73 (0.03)	0.02*	0.50	0.49

Values are reported as means (SD).
*Statistically significant.
AR, aspect ratio; BPR, beam-to-pore ratio; CTVF, connective tissue volume fraction, Inf, inferior; Sup, superior; Temp, temporal.

Table 3. LC Microstructural Measurements in Depth

Parameter	Anterior	Middle	Posterior	*P* Value		
				Ant vs. Mid	Ant vs. Post	Mid vs. Post
Beam thickness, µm	32.65 (3.99)	34.54 (3.22)	33.56 (3.20)	0.04*	0.09	0.62
Pore diameter, µm	20.70 (3.12)	22.05 (3.17)	21.96 (2.65)	<0.01*	<0.01*	0.91
Pore area, µm	828.55 (225.16)	905.39 (247.26)	890.50 (222.38)	<0.01*	0.02*	0.49
Pore AR	1.95 (0.08)	1.92 (0.09)	1.94 (0.10)	0.74	0.36	0.68
BPR	1.60 (0.22)	1.58 (0.19)	1.54 (0.17)	0.27	0.03*	0.54
CTVF, %	0.74 (0.03)	0.74 (0.03)	0.75 (0.03)	0.53	0.26	0.19

Values are reported as means (SD).
*Statistically significant.
AR, aspect ratio; BPR, beam-to-pore ratio; CTVF, connective tissue volume fraction.

$P = 0.02$; see Table 1). No significant difference was detected between the center and periphery for any of the other parameters.

Quadrants

The temporal quadrant was considerably more visible than all other quadrants (temporal = 59.5%, superior = 23.3%, and inferior = 23.3%). The nasal quadrant was excluded from the quadrant analysis due to low visibility. BPR and CTVF were significantly smaller in the inferior compared with the superior quadrant (Table 2). The pore area was marginally significantly smaller ($P = 0.05$) in the superior quadrant compared with the inferior. No significant difference was detected for any of the other parameters. None of the temporal measurements was significantly different from either superior or inferior measurements.

Depth

The depth-resolved analysis demonstrated significant differences in several parameters (Table 3). The anterior LC has a significantly smaller beam thickness, pore diameter, and pore area than the middle third. Pore diameter and pore areas of the anterior LC were smaller, and BPR was larger than the posterior third of the lamina. There was no statistically significant difference in any of the parameters between the middle and posterior regions.

Correlation Among Parameters

To test the relationship between structural features of the LC, we investigate the correlation among global LC parameters (Table 4). Pore diameter and pore areas were both positively correlated with disc area ($r = 0.51$, $P = 0.04$; $r = 0.69$, $P < 0.01$, respectively), with larger pores in larger discs and vice versa. Beam thickness was positively correlated to pore diameter ($r = 0.62$, $P = 0.01$). At the same time, BPR was negatively correlated with pore diameter ($r = –0.74$, $P < 0.01$) and area ($r = –0.83$, $P < 0.01$), with no significant correlation detected with beam thickness ($P = 0.82$). CTVF was positively correlated with BPR ($r = 0.67$, $P < 0.01$) and consecutively negatively correlated with pore area and AR ($r = –0.58$, $P = 0.02$; $r = –0.75$, $P < 0.001$, respectively).

Table 4. Spearman's Correlation Coefficients Between LC Microstructural Measurements

	Pore Diameter	Pore Area	Pore AR	BPR	CTVF	Disc Area
Beam thickness	0.62 (0.01)*	0.30 (0.25)	−0.46 (0.07)	0.06 (0.82)	0.47 (0.07)	0.27 (0.32)
Pore diameter		0.87 (<0.01)*	0.05 (0.86)	−0.74 (<0.01)*	−0.24 (0.38)	0.51 (0.04)*
Pore area			0.39 (0.14)	−0.83 (<0.01)*	−0.58 (0.02)*	0.69 (<0.01)*
Pore AR				−0.46 (0.07)	−0.75 (<0.01)*	0.13 (0.63)
BPR					0.67 (<0.01)*	−0.41 (0.12)
CTVF						−0.36 (0.17)

*Statistically significant.
BPR, beam-to-pore-ratio; AR, aspect ratio; CTVF, connective tissue volume fraction.

Discussion

In the present study, we characterized in vivo the LC structure in 3D of healthy NHP using OCT. These measurements provide the most comprehensive in vivo LC microstructure analysis and lay the foundation for future works that aim to understand changes due to disease state. Several statistically significant regional structural differences were detected between the center and periphery, between quadrants, and with depth. Past studies have used in vivo OCT and adaptive optics scanning laser ophthalmoscopy with manual marking of the anterior LC structures[15] and light microscopy[16] to quantify LC pore sizes and shapes in monkeys. These studies were limited to the anterior LC surface or use manual segmentation with reduced reproducibility compared to automated segmentation,[12] as used in the current study. Some studies have shown that ocular histology is comparable to OCT data.[17,18] However, those studies mostly focused on comparing gross structures of LC and macula landmarks and primarily along the axial direction. This direction has the highest sampling density and resolution in OCT. The LC microstructure measurements should consider lateral and axial resolution where lateral resolution in OCT is markedly lower than the axial resolution (except for adaptive optics OCT devices).

The beams at the central lamina were significantly thicker than the beams of the periphery (see Table 1). This distinction agrees with a previous histologic study on 21 NHPs,[8] where the central beams were 8% thicker than the periphery compared with 9% thicker in our study. Furthermore, the mean central pore diameter was 5% larger than the periphery in the previous histology study compared with 7% larger in our study. However, unlike histology, this difference was not statistically significant in our study, perhaps due to the smaller sample size or the reduced visibility. This finding contradicts previous histology reports in humans where the largest pores on the lamina's anterior surface are in the periphery.[19] However, our results agree with an in vivo study evaluating human LC in 3D.[20] The discrepancy might be due to the analysis of the LC in 3D compared to only analyzing the lamina's anterior surface.

We did not detect any significant difference between quadrants' measurements, except between the superior and inferior quadrants (see Table 2). This finding contradicts several ex vivo studies demonstrating larger beams in the temporal quadrant.[8,16,19,21,22] Several studies have shown that the superior and inferior quadrants feature larger pores as the thicker arcuate nerve bundles traverse those regions.[8,16,21] Our study did not detect such differences, and this might be due to several reasons. Reduced visibility of the superior and inferior sectors, compared to the temporal, might provide an incomplete representation of those sectors. Second, the known intersubject variability in major retinal nerve bundle locations can obscure sectoral differences when analyzing a relatively small number of eyes.[23,24] Third, in Lockwood et al.'s comprehensive histomorphometric study, the largest pore diameter was found superior-temporally and inferior-temporally according to their clock-hours LC analysis.[8] This difference might also be due to the comparison of ex vivo and in vivo measurements, the use of manual segmentation, subjective assessment, the use of different quantification methods than those used in our study or represent a limitation of the LC quantification we provide herein but offer the actual reality for future reference of OCT in vivo analysis of the lamina.

Analyzing the LC depth-wise, the anterior LC had significantly thinner beams than the middle LC (see Table 3). This microstructural difference was supported by NHP and human histology.[8,16] Nadler et al. used adaptive optics OCT to characterize the living human LC microstructure and reported similar findings.[20] In addition to thinner beams, we also noticed that the anterior LC had smaller pores than the middle LC,

which was also reported in humans.[20] However, in histology, the middle segment had smaller pores than the anterior.[8] In both NHP histology and human OCT, the posterior region was structurally similar to the anterior part,[8,20] whereas we reported similarity between the middle and the posterior regions. This later similarity in measurements reduces the possibility that our measurements from deeper structures are affected by reduced signal and quality. According to our results, where both beams and pores are smaller in the anterior third than the two deeper thirds, it seems that the lamina is squeezed anteriorly, probably by the scleral opening, and then expands toward the optic nerve. Alternatively, it is constructed by smaller beams and having smaller pores than the deeper parts of the LC.

When examining the relationship among LC parameters, we reported that the optic disc area was positively correlated with pore diameter and area but no significant correlation with beam thickness (see Table 4). In other words, larger discs are associated with larger pores but not with larger beams. This counterintuitive finding is further emphasized when considering the significant positive correlation between pore diameter and beam thickness, where larger pore requires larger beams to support them. These findings are likely because disc area is a 2D measurement where both beam thickness and pore diameter are pure 3D parameters. Fitting the best-fitting sphere into a highly irregular 3D structure, such as the LC pore and beam, measures the largest space within this complex structure but does not capture the full structure's intricacy. Conversely, this 3D quantification approach is less prone to large measurement variability due to varying scan angle, as commonly seen with OCT scanning, than most other parameters. We have also noted that CTVF is correlated with pore area and pore AR, but no significant correlation was detected with either beam thickness or pore diameter. BPR is negatively correlated with all pore parameters, as expected, with no significant correlation with the beam thickness.

There are some limitations to consider when interpreting the results of our study. First, our sample size was small, as is usually the case in NHP studies, for obvious humane reasons. Nonetheless, we were still able to detect statistically significant differences. Second, as in any in vivo OCT study of the LC, visibility is limited and variable. However, LC visibility in our research was similar to past in vivo OCT studies.[11,20] Third, some image processing (smoothing and contrast enhancement) was subjectively performed to each eye to ensure that the segmentation algorithm accomplishes the most accurate LC microstructure delineation. Fourth, our method is only semi-automatic, as the selection of the areas of visible LC was subjectively performed. Nonetheless, both processes were carried out by two experienced investigators prior to performing any quantified analysis. Fifth, dividing a complex structure, such as the lamina, into sectors inevitably leads to some structures being split into two parts, one in each sector. Although this might impair comparison with the biological structure of the lamina, this should not bias the comparison between sectors one way or another. Furthermore, this information will be useful for those interested in sectoral analysis of the lamina, as their measurements will be prone to the same limitation. Finally, there is an inherent limitation in BoneJ measurements. Large pores include more voxels to represent their size than small pores, which leads to over-representation of large pores and beams in globally averaged values. The measurements need to be compensated for the number of voxels involved to represent each pore to calculate more accurate global mean values. Because this procedure requires recognizing individual pores with their particularly associated voxels, pore segmentation needs to be incorporated within the BoneJ method, which currently does not exist. This limitation is more complicated for the beam measurement because they are all connected, so that skeletonized beam structure with associated voxel assignment needs to be recognized to calculate the global mean correctly. Further investigation is warranted.

In conclusion, we have utilized a semi-automated segmentation method to describe the in vivo, healthy NHP LC microarchitecture. We detected mostly small but statistically significant structural differences between various regions within the lamina. As we continue exploring the LC's role in ocular diseases, identifying its structure in healthy eyes is essential. Looking forward, the findings of this study will serve as a reference for future in vivo, NHP, disease-associated LC changes.

Acknowledgments

The authors thank MA Smith, PhD, from the Department of Biomedical Engineering and Neuroscience Institute, Carnegie Mellon University, Pittsburgh, PA, for his assistance in animal handling.

Supported by NIH R01-EY030770, R01-EY025011, and R01-EY013178 (Bethesda, MD), and an unrestricted grant from Research to Prevent Blindness (New York, NY).

Conflict of Interest: J.S. Schuman receives royalties for intellectual property licensed by the Massachusetts Institute of Technology and Massachusetts Eye and Ear Infirmary to Zeiss.

Disclosure: **A. Sainulabdeen,** None; **Y. Glidai,** None; **M. Wu,** None; **M. Liu,** None; **P. Alexopoulos,** None; **H. Ishikawa,** None; **J.S. Schuman,** Zeiss (R); **G. Wollstein,** None

[*] AS and YG contributed equally in the preparation of the manuscript.

References

1. Downs JC, Girkin CA. Lamina cribrosa in glaucoma. *Curr Opin Ophthalmol*. 2017;28(2):113–119.
2. Quigley H, Anderson DR. The dynamics and location of axonal transport blockade by acute intraocular pressure elevation in primate optic nerve. *Invest Ophthalmol*. 1976;15(8):606–616.
3. Hernandez MR. The optic nerve head in glaucoma: role of astrocytes in tissue remodeling. *Prog Retin Eye Res*. 2000;19(3):297–321.
4. Burgoyne CF. A biomechanical paradigm for axonal insult within the optic nerve head in aging and glaucoma. *Exp Eye Res*. 2011;93(2):120–132.
5. Wang B, Tran H, Smith MA, et al. In-vivo effects of intraocular and intracranial pressures on the lamina cribrosa microstructure. *PLoS One*. 2017;12(11):e0188302.
6. Burgoyne CF. The non-human primate experimental glaucoma model. *Exp Eye Res*. 2015;141: 57–73.
7. Rasmussen CA, Kaufman PL. Primate glaucoma models. *J Glaucoma*. 2005;14(4):311–314.
8. Lockwood H, Reynaud J, Gardiner S, et al. Lamina cribrosa microarchitecture in normal monkey eyes part 1: methods and initial results. *Invest Ophthalmol Vis Sci*. 2015;56(3):1618–1637.
9. Reynaud J, Lockwood H, Gardiner SK, et al. Lamina Cribrosa Microarchitecture in Monkey Early Experimental Glaucoma: Global Change. *Invest Ophthalmol Vis Sci*. 2016;57(7):3451–3469.
10. Yang H, Reynaud J, Lockwood H, et al. 3D Histomorphometric Reconstruction and Quantification of the Optic Nerve Head Connective Tissues. *Methods in Molecular Biology (Clifton, NJ)*. 2018;1695:207–267.
11. Nadler Z, Wang B, Wollstein G, et al. Automated lamina cribrosa microstructural segmentation in optical coherence tomography scans of healthy and glaucomatous eyes. *Biomedical Optics Express*. 2013;4(11):2596–2608.
12. Wang B, Nevins JE, Nadler Z, et al. Reproducibility of in-vivo OCT measured three-dimensional human lamina cribrosa microarchitecture. *PLoS One*. 2014;9(4):e95526.
13. Schindelin J, Arganda-Carreras I, Frise E, et al. Fiji: an open-source platform for biological-image analysis. *Nature Methods*. 2012;9(7):676–682.
14. Doube M, Kłosowski MM, Arganda-Carreras I, et al. BoneJ: Free and extensible bone image analysis in ImageJ. *Bone*. 2010;47(6):1076–1079.
15. Ivers KM, Sredar N, Patel NB, et al. In Vivo Changes in Lamina Cribrosa Microarchitecture and Optic Nerve Head Structure in Early Experimental Glaucoma. *PLoS One.* 2015;10(7):e0134223.
16. Radius RL, Gonzales M. Anatomy of the Lamina Cribrosa in Human Eyes. *Arch Ophthalmol*. 1981;99(12):2159–2162.
17. Strouthidis NG, Grimm J, Williams GA, et al. A comparison of optic nerve head morphology viewed by spectral domain optical coherence tomography and by serial histology. *Invest Ophthalmol Vis Sci*. 2010;51(3):1464–1474.
18. Anger EM, Unterhuber A, Hermann B, et al. Ultrahigh resolution optical coherence tomography of the monkey fovea. Identification of retinal sublayers by correlation with semithin histology sections. *Exp Eye Res*. 2004;78(6):1117–1125.
19. Jonas JB, Mardin CY, Schlotzer-Schrehardt U, et al. Morphometry of the human lamina cribrosa surface. *Invest Ophthalmol Vis Sci*. 1991;32(2):401–405.
20. Nadler Z, Wang B, Schuman JS, et al. In vivo three-dimensional characterization of the healthy human lamina cribrosa with adaptive optics spectral-domain optical coherence tomography. *Invest Ophthalmol Vis Sci*. 2014;55(10):6459–6466.
21. Radius RL. Regional specificity in anatomy at the lamina cribrosa. *Arch Ophthalmol*. 1981;99(3):478–480.
22. Winkler M, Jester B, Nien-Shy C, et al. High resolution three-dimensional reconstruction of the collagenous matrix of the human optic nerve head. *Brain Res Bull*. 2010;81(2-3):339–348.
23. Swanson WH, King BJ, Burns SA. Within-subject variability in human retinal nerve fiber bundle width. *PLoS One*. 2019;14(10):e0223350.
24. Kocaoglu OP, Cense B, Jonnal RS, et al. Imaging retinal nerve fiber bundles using optical coherence tomography with adaptive optics. *Vision Res*. 2011;51(16):1835–1844.